Catalytic hydropyrolysis of biomass using supported CoMo catalysts – Effect of metal loading and support acidity

Stummann, Magnus Zingler; Elevera, Elaine; Hansen, Asger Baltzer; Hansen, Lars Pilsgaard; Beato, Pablo; Davidsen, Bente; Wiwel, Peter; Gabrielsen, Jostein; Jensen, Peter Arendt; Jensen, Anker Degn

Total number of authors:
11

Published in:
Fuel

Link to article, DOI:
10.1016/j.fuel.2019.116807

Publication date:
2020

Document Version
Peer reviewed version

Catalytic hydropyrolysis of biomass using supported CoMo catalysts – Effect of metal loading and support acidity

Magnus Zingler Stummann[a], Elaine Elevera[a], Asger Baltzer Hansen[b], Lars Pilsgaard Hansen[b], Pablo Beato[b], Bente Davidsen[b], Peter Wiwel[b], Jostein Gabrielsen[b], Peter Arendt Jensen[a], Anker Degn Jensen[a], Martin Høj[a*]

[a]*Department of Chemical and Biochemical Engineering, Technical University of Denmark (DTU), DK-2800 Kgs. Lyngby (Denmark)*

[b]*Haldor Topsoe A/S, 2800 DK-Kgs. Lyngby (Denmark)*

**mh@kt.dtu.dk*

Abstract

Catalytic hydropyrolysis of biomass to green fuels was performed using supported, sulfided CoMo catalysts. With $MgAl_2O_4$ as support material the CoMo loading was varied between 4.1 and 12.0 wt.% at constant Co/Mo atomic ratio of 0.3. Increasing the metal loading decreased the amount of oxygen in the condensed organic phase from 9.0 to 4.7 wt.% on dry basis (db) and the condensable organic yield decreased from 25.2 to 22.7 wt.% on dry ash free (daf) basis, corresponding to a decrease in the carbon recovery from 39 to 37 %. Using zeolite H-ZSM-5 mixed with alumina as support with a CoMo loading of 4.1 wt.%, the condensed organics contained only 5.2 to 6.1 wt.% db oxygen. The condensable organic yield was between 23.9 and 24.4 wt.% db, and the carbon recovery was 39-40 %. Thus using an acidic support can remove the oxygen without decreasing the carbon recovery. The latter was ascribed to alkylation of the aromatics when the zeolite support was used.

Elemental maps of the spent catalysts were obtained using STEM-EDS, showing that the CoMo phase was mainly located as monolayer MoS_2 slab structures (>93 %) on the support and indicated a high dispersion of cobalt, consistent with incorporation of Co into the MoS_2 structure in the CoMoS phase. Potassium was

observed on all the spent catalysts, indicating transfer of alkali metal from the biomass to the catalyst. Potassium may decrease the acidity of the catalyst over time, thus reducing the positive effect of using a more acidic support.

Keywords: biomass; molybdenum sulfide; hydrodeoxygenation; zeolite; biofuel

Abbreviations

AED	Atomic emission detector
BET	Brunauer–Emmett–Teller
CUS	Coordinatively unsaturated sites
daf	Dry, ash free basis
db	Dry basis
DDO	direct deoxygenation
diAro	Diaromatics
EDS	Energy dispersive X-ray spectroscopy
FB	Fluid bed
FCC	Fluid catalytic cracking
FID	Flame ionization detector
GC	Gas chromatograph
HAADF	High-angle annular dark-field
HDO	Hydrodeoxygenation
HYD	Hydrogenation
ICP-OES	Inductive coupled plasma optical emission spectroscopy
mAro	Monoaromatics
MgAl	$MgAl_2O_4$
MS	Mass spectrometry
Naph	Naphthenes
O-Ali	Oxygenated aliphatics
O-Aro	Larger oxygenated aromatics
Par	Paraffins

PhOH	Phenolics
Ph(OH)2	Dihydroxybenzene
SSA	Specific surface area
SEM	Scanning electron microscopy
STEM	Scanning transmission electron microscopy
TAN	Total acid number
Temp.	Temperature
TPD	Temperature programmed desorption
tetAro+	Tetra- and higher aromatics
triAro	Triaromatics
ZA	H-ZSM-5 mixed with Al_2O_3

29

1 Introduction

The current production and consumption of energy is responsible for 60 % of the global greenhouse gas (GHG) emissions [1], which is responsible for global warming [2], and the global energy consumption will most likely continue to increase in the near future [3]. The current greenhouse gas emission targets aim at a temperature rise of no more than 2°C, however, even a global average temperature increase of 2°C can lead to multi-meter sea level rise [2,4], and thus it is evident that the emissions of GHG must be drastically decreased immediately. One way of decreasing our GHG emission is to use thermochemical conversion of lignocellulosic biomass for the production of liquid, second-generation bio-fuels. Recent research by Marker et al. [5,6] indicated that catalytic hydropyrolysis is an very efficient method for production of bio-gasoline and -diesel. With their process, called IH$^{2®}$, they produced an oxygen free oil (oxygen<1 wt.%) with a condensable organic yield (condensed organics and C_{4+} in the gas) between 25.8 and 29.5 wt.% dry ash free (daf) for woody biomass [5,6]. In the IH$^{2®}$ process, pyrolysis of the biomass and hydrodeoxygenation (HDO) of the formed oxygenates takes place simultaneously in a fluid bed reactor. Remaining oxygenates are converted in a downstream, fixed bed HDO reactor. Life cycle assessments of catalytic hydropyrolysis of biomass have shown that this technology can decrease the GHG emissions of liquid transportation fuels with between 30-96 % compared to the fossil counterparts, depending on the type of biomass feedstock, with bagasse giving the largest reduction [7–9]. Furthermore, thermodynamic analysis of polygeneration systems based on catalytic hydropyrolysis has shown that it is possible obtain an energy efficiency of the overall process of 89 % (LHV) [10].

Other groups have also investigated catalytic hydropyrolysis. Dayton et al. [11–13] investigated catalytic hydropyrolysis of woody biomass in a fluid bed reactor at 375-500 °C and between 1 and 31 bar hydrogen pressure and tested several pre-reduced catalysts. At 1 bar and 450 °C and using a molybdenum-based reduced metal catalyst they were able to achieve a carbon recovery for the condensed organics and C_{4+} of 43.0 % with an oxygen content in the organic phase of 6.2 wt.% dry basis (db) [13]. However, they did not

report the catalyst composition. Gamliel et al. [14–16] investigated the effect of pressure and catalyst properties in catalytic hydropyrolysis using a Pyroprobe reactor. Testing different supports (H-ZSM-5, SiO_2, Al_2O_3) showed that the Brønsted acidity was important for the oxygen removal and could decrease the char formation by catalyzing decarbonylation and aromatization of the oxygenates, thus minimizing secondary condensation reactions [15]. This observation has also been confirmed by Chandler and Resende, who conducted catalytic hydropyrolysis using H-ZSM-5 in a fluid bed reactor [17]. However, it should be noted that too high acidity can also lead to polymerization and coke formation [15]. Several other research groups have also used H-ZSM-5 in catalytic hydropyrolysis both as a catalyst [18–23] and as support [19–21,24]. Using H-ZSM-5 as support and impregnating it with different metals (Ni, Co, Mo, Pt, Ru and Pd) generally increases the aromatic yield [15,19,20].

Limited research within catalytic hydropyrolysis is conducted with sulfided CoMo, NiMo and Mo catalysts. These catalysts are normally used for hydrotreating crude oil, and have the advantage, compared to most reduced metal catalysts, that they are sulfur tolerant [25]. This is important because most biomass sources contains sulfur (0.03-3.4 wt.% db) [26]. Furthermore, it is well-known that these catalysts are active and fairly stable in hydrodeoxygenation of model compounds and real bio-oil [27–35]. Adding a promoter (Co or Ni) to MoS_2 leads to an increased formation of coordinatively unsaturated sites (CUS) [36–38], thereby increasing the deoxygenation activity [32,39]. One important difference between the two promoters is that NiMoS mainly removes oxygen through the hydrogenation (HYD) pathway, where the aromatic ring is hydrogenated prior to the removal of oxygen, while CoMoS mainly removes oxygen without hydrogenating the aromatic ring, thus following the direct deoxygenation (DDO) pathway [33,39–42]. However, at the temperatures commonly applied in catalytic hydropyrolysis (400 to 500 °C) the (mono)aromatics are favored by equilibrium [43], inhibiting the HYD pathway, thus making Co the better promoter. We have previously confirmed this experimentally [44].

We have previously investigated the effect of the catalyst in the fluid bed reactor [45] and obtained a condensable oil yield (condensed organics and C_{4+}) of 24.0 wt.% daf with a NiMo/H-ZSM-5 mixed with Al_2O_3, while using a CoMo/$MgAl_2O_4$ catalyst gave a condensable organic yield of 21.5 wt.%. A fixed bed HDO reactor with a NiMo/Al_2O_3 catalyst was used after the fluid bed reactor and the condensed organics contained less than 0.2 wt.% oxygen. However, the commercial catalysts used in that study could not be characterized in detail and it was not possible to determine the reason for the high yield with NiMo/H-ZSM-5 mixed with Al_2O_3.

In this study, we investigated the effect of the CoMo loading and the effect of the support acidity on the product distribution and deoxygenation activity. In order to obtain a thorough understanding of the effect of the catalyst properties on the products, the calcined oxide precursors were characterized with Raman spectroscopy, NH_3-TPD and the BET surface area was measured by nitrogen physisorption and the spent catalysts were characterized with scanning and scanning transmission electron microscopy (SEM and STEM). Furthermore, the liquid products were extensively analyzed.

2 Material and methods

2.1 Biomass feedstock

The biomass feedstock was bark free beech wood, which contained 6.72 wt.% moisture and 0.59 wt.% on dry basis (db) ash. The elemental composition can found elsewhere [43].

2.2 Catalyst preparation

The catalysts were prepared by sequential incipient wetness impregnation on three different support materials, supplied by Haldor Topsøe A/S. $MgAl_2O_4$ (MgAl) was used as support for testing the effect of the CoMo loading and two supports consisting of zeolite (H-ZSM-5) mixed with alumina, denoted as ZA#1 and ZA#2, were used for testing the effect of the support acidity. ZA#2 consisted of 44 % more H-ZSM-5 than ZA#1. The supports were crushed to obtain particle sizes of 180-355 µm, to obtain a good fluidization of the

bed. Prior to the impregnation, MgAl was calcined in air for 10 hours and in order to keep the Mo/nm^2 surface loading constant, the calcination temperature was varied (see Table 1) and the calcined MgAl had a specific surface area (SSA) between 56 and 200 m^2/g. In order to maintain the properties of the zeolite based supports, ZA#1 and ZA#2, were not calcined prior to the impregnation. The supports had a pore volume between 0.60 and 0.95 g_{water}/g.

Table 1 Calcination temperature, specific surface area, and pore volume of the used catalyst support materials.

Support	Calcination temp. (°C)	BET SSA (m^2/g)	Pore volume (g_{water}/g)
MgAl#1	995	56	0.62
MgAl#2	905	96	0.82
MgAl#3	800	143	0.91
MgAl#4	600	200	0.95
ZA#1	-	ND	0.69
ZA#2	-	ND	0.60

The support was impregnated with an aqueous solution (corresponding to 110 % the pore volume) of $(NH_4)_6Mo_7O_{24}\cdot 4H_2O$ (Fluka≥99.0%), aged by stirring for ~3 hours and dried overnight at ~ 110 °C in air. A second impregnation with $Co(NO_3)_2\cdot 6H_2O$ (Fluka ≥ 98%) was conducted using the same procedure. The calcination was conducted with an air flow of 1.24-1.30 NL/min technical air (20% O_2 in N_2) at 500°C (ramp: 5°C/min) and holding for 3 hours. The calcined catalysts were sieved to 180-355 µm again to remove any agglomerates or dust formed during the catalyst preparation. An estimated Mo loading between 3.3 and 3.4 atoms/nm^2 (see Table 2) was obtained for CoMoMgAl#1 – #3, while it was 4.7 atoms/nm^2 for CoMoMgAl#4. The higher surface loading for CoMoMgAl#4 was due to a significant decrease in the surface area from 200 to 148 m^2/g during the second calcination, possibly due to pore blocking during the preparation. Loadings lower than 4 atoms/nm^2 corresponds to a sub monolayer dispersion of Mo-oxide on $MgAl_2O_4$, assumed similar to γ-Al_2O_3 [46], which should lead to a high dispersion of smaller MoS_2 particles (when sulfided) with a moderate activity, thus minimizing the formation of the highly active type II sites [47]. The loading for CoMoZA#1 was 0.71 atoms/nm^2 and the loading for CoMoZA#2 was 0.60 atoms/nm^2. The Co to Mo molar ratio was aimed at 0.3, which should ensure that the less active Co_9S_8 phase is not formed [48].

120 Prior to the experiment the catalysts were sulfided in-situ in the catalytic hydropyrolysis setup at 26 bar,
121 350°C with 1.8 mol % H_2S as described elsewhere [44].

122 **Table 2 Composition of the calcined oxide catalyst precursors**

Catalyst	Mo (wt.%)	Co (wt.%)	Co/Mo (molar)	Mo load (Atoms/nm^2)	BET SSA (m^2/g)
CoMoMgAl#1	3.41	0.64	0.30	3.6	60
CoMoMgAl#2	5.58	0.99	0.29	3.4	102
CoMoMgAl#3	7.74	1.49	0.31	3.3	136
CoMoMgAl#4	10.1	1.86	0.30	4.7	148
CoMoZA#1	3.61	0.67	0.29	0.71	319
CoMoZA#2	3.39	0.60	0.29	0.60	354

123 ## 2.3 Experimental setup and procedure

124 The experiments were conducted in a bench scale catalytic hydropyrolysis setup (see Figure 1), which is
125 described in detail elsewhere [43]. In brief, the setup consisted of a gas feeding system (H_2 flow: 82 Nl/min,
126 N_2 flow: 5 Nl/min), a biomass feeding system (feeding rate: 270-282 g/h), a fluid bed reactor (operated at
127 450 °C), followed by a filter for char removal, a condensation system, and an online GC measuring the gas
128 composition every 10 min. The total experimental time was between 2.5 and 3.5 h, and the char and
129 condensed liquids were first collected after the experiment was completed. The experimental error for the
130 solids (char and coke), C_1-C_3, total CO and CO_2, aqueous phase, and condensable organics (condensed
131 organics and C_{4+} in the gas) were previously determined to 0.5, 0.2, 0.5, 1.5, and 0.5 wt.% daf, respectively
132 [45].

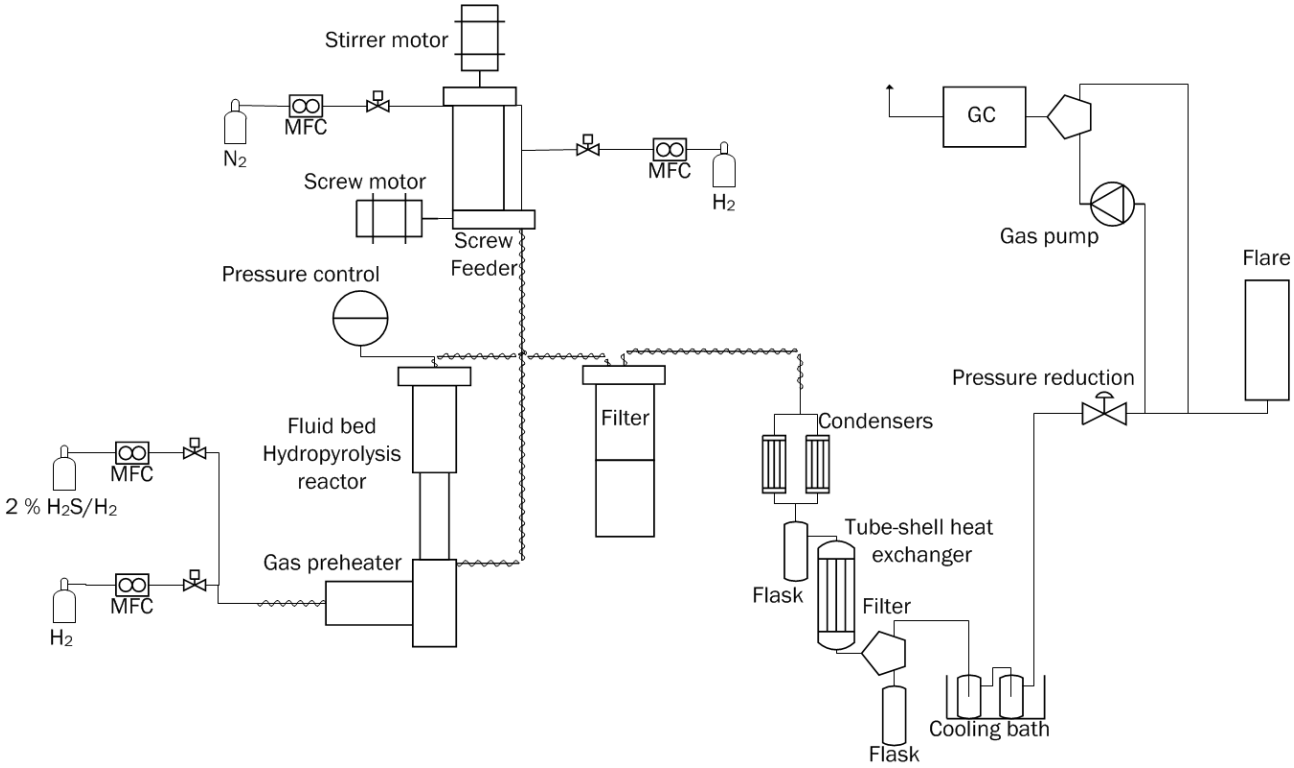

133

134 **Figure 1. Simplified piping and instrumentation diagram of the catalytic hydropyrolysis setup. Reprinted with permission from**

135 [44]**. Copyright 2019 American Chemical Society.**

136 2.4 Liquid phase analysis methods

137 The condensed organic phase was extensively characterized as described in detailed elsewhere [43–45]. The

138 hydrogen and sulfur contents were measured using ASTM method D7171 and D4292. The density was

139 measured according to ASTM D4052 and oxygen content was measured with a Flash 2000 elemental analyzer

140 at DB Lab A/S. The water content in the organic phase was measured with Karl Fisher titration and the total

141 acid number (TAN) was measured by titration with KOH at DB lab A/S. The condensed organic phase was also

142 analyzed with GC×GC-ToF/MS and sulfur specific GC-AED.

143 Carbon specific GC-AED was used to determine the carbon content in the aqueous phase, and the organic

144 compounds were identified by use of GC-MS/FID as described elsewhere [45,49].

145

2.5 Catalyst characterization

Several methods were used to characterize the fresh and spent catalysts and detailed descriptions can be found elsewhere [45,49]. The composition (cobalt, molybdenum) of the calcined oxide catalyst precursors were determined using inductive coupled plasma optical emission spectroscopy (ICP-OES) when MgAl was used as support material and wavelength dispersive X-ray fluorescence (WD-XRF) when H-ZSM-5 mixed with alumina was used as support material. The surface area of the calcined oxide catalyst precursors were measured with N_2-physisorption (BET). The acidity was measured using temperature programmed ammonia desorption (NH_3-TPD). Raman spectroscopy on the samples was performed at ambient conditions. The samples were both analyzed in a fluidized bed set-up, as described by Beato et al. [50]**,** and at different spatial spots.

The carbon and potassium contents on the spent catalysts were measured using scanning electron microscopy (SEM) equipped with an EDS detector. Transmission electron microscopy was used to determine the slab length and the degree of stacking. Elemental maps were obtained in scanning transmission mode (STEM) and used investigate the potassium and calcium on the spent catalysts. A detailed description of the used methods can be found elsewhere [45,49].

3 Results and Discussion

A summary of reaction conditions, mass balances, and properties of the condensed liquids is shown in Table 3. The mass balance closed between 97.8 and 100.4 wt.% daf, the feeding rate varied between 270 and 282 g/h, and the feeding time varied between 2.5 and 3.5 hours. The liquid phases from experiment 2 were contaminated and were therefore not analyzed. A detailed gas composition is provided in the supplementary information, Table S.1. It should be noted that the results from experiment 1 has previously been published [44], and are included here as reference. The carbon recovery was defined as the carbon in the product divided with the carbon in biomass multiplied by 100 and the C_{4+} efficiency was defined as the sum of the carbon recovery in C_{4+} gasses and the condensed organic phase.

Table 3 Summary of reaction conditions and mass balance for catalytic hydropyrolysis of beech wood in a fluid bed reactor with sulfided CoMo catalysts with different loadings and using different supports.

Test	1	2	3	4	5	6
Test conditions						
FB temperature (°C)	451	450	454	450	454	454
FB catalyst	CoMoMgAl#1	CoMoMgAl#2	CoMoMgAl#3	CoMoMgAl#4	CoMoZA#1	CoMoZA#2
Pressure (bar)	26	26	26	26	26	26
Feed time (h)	3.5	3.5	3.4	3.4	3.5	2.5
Feeding rate (g/h)	275	275	280	276	270	282
H_2S conc.(ppm)	460	460	460	460	460	460
H_2 flow (NL/min)	82	82	82	82	82	82
N_2 flow (NL/min)	5	5	5	5	5	5
Yields (wt. daf %)						
Gas	26.1	28.8	30.8	29.7	27.9	30.0
Char + coke	13.3	13.0	13.1	13.2	13.0	13.3
Aqueous phase	33.3	33.2	32.6	33.1	33.1	33.2
Organic phase	17.7	13.4	12.1	11.9	14.3	14.0
C_{4+} in the gas	7.5	10.1	10.6	10.8	10.1	9.9
Organics + C_{4+}	25.2	23.5	22.7	22.7	24.4	23.9
Mass balance	97.8	98.5	99.2	98.8	98.8	100.4
Carbon recovery (%)						
C_1-C_3	19	23	25	24	25	27
C_{4+}	13	17	18	18	17	17
CO+CO_2	11	11	12	11	11	11
Organic phase	26	ND	18	18	22	22
Aqueous phase	3.2	ND	1.1	0.97	0.67	0.97
C_{4+} efficiency	39	ND	36	37	40	39
Organic phase composition						
Water (wt.%)	3.3	ND	1.6	1.2	1.3	1.3
C* (wt.% db)	81	ND	84	85	85	85
H (wt.% db)	9.39	ND	9.56	9.70	9.30	8.99
O (wt.% db)	9.0	ND	6.2	4.7	5.2	6.1
S (wt.% db)	0.22	ND	0.27	0.27	0.18	ND
Organic phase physical properties						
Density at 40°C (g/ml)	0.9428	ND	0.9308	0.9185	0.9511	0.9515
TAN (mg_{KOH}/g)	4.00	ND	0.40	0.30	ND	0.60
Aqueous phase composition (wt.%)						
C	4.3	ND	1.5	1.3	0.9	1.3
Gas composition (wt.% daf)						
CO	6.5	8.3	8.9	8.9	6.7	7.7
CO_2	9.2	7.7	7.8	8.9	8.3	8.4
C_1-C_3	10.3	12.7	14.1	14.0	13.0	13.9
C_{4+}	7.5	10.1	10.6	10.8	10.1	9.9

*By difference

3.1 Product distribution

The product distribution is shown in Figure 2. The condensable organic yield decreased from 25.2 to 22.7 wt.% daf when the CoMo loading was increased from 4.1 to 12.0 wt.%, see Figure 2(A). Likewise the condensable organic yield decreased from 25.2 to 24.4 and 23.9 wt.% daf when CoMoMgAl#1 was replaced with the similarly CoMo loaded CoMoZA#1 and CoMoZA#2, respectively. Thus, only a minor difference was observed between CoMoZA#1 and CoMoZA#2. The total gas yield, shown in Figure 2(B), increased with the

CoMo loading from 26.1 wt.% daf when the CoMo loading was 4.1 wt.% to 30.8 wt.% daf when the CoMo loading was increased to 9.2 wt.%. Further increasing the CoMo loading to 12.0 wt.% slightly decreased the total gas yield to 29.7 wt.% daf, due to a decrease in the CO and CO_2 yield. The total CO and CO_2 yield varied between 15.8 and 16.7 wt.% daf when the CoMo loading was varied, thus almost constant. The C_1-C_3 yield increased from 10.3 to 14.1 wt.% daf when the CoMo loading was increased from 4.1 to 9.2 wt.%, but remained constant for 12.0 wt.% CoMo . The total gas yield also increased when CoMoZA#1 (27.9 wt.% daf) and CoMoZA#2 (30.0 wt.% daf) was used instead of CoMoMgAl#1 (26.1 wt.%). This was due to an increased yield of C_1-C_3, which was 10.3 wt.% daf for CoMoMgAl#1, 13.0 wt.% daf for CoMoZA#1 and 13.9 wt.% daf for CoMoZA#2. CoMoZA#2 (higher acidity) produced more CO, CO_2 and C_1-C_3 than CoMoZA#1. The char and coke yield varied between 13.0 and 13.3 wt.%, thus the variations were within the experimental uncertainty, which indicates that the char and coke yield are independent of the CoMo loading and the support acidity, in the tested range. Likewise, the variations in the aqueous phase yield between 32.6 and 33.3 wt.% daf was within the experimental uncertainty.

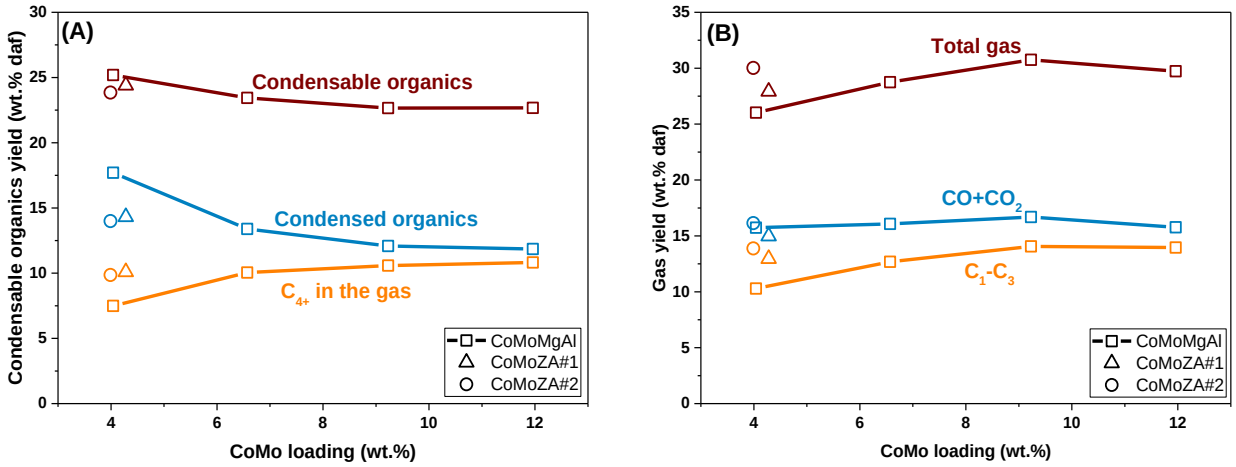

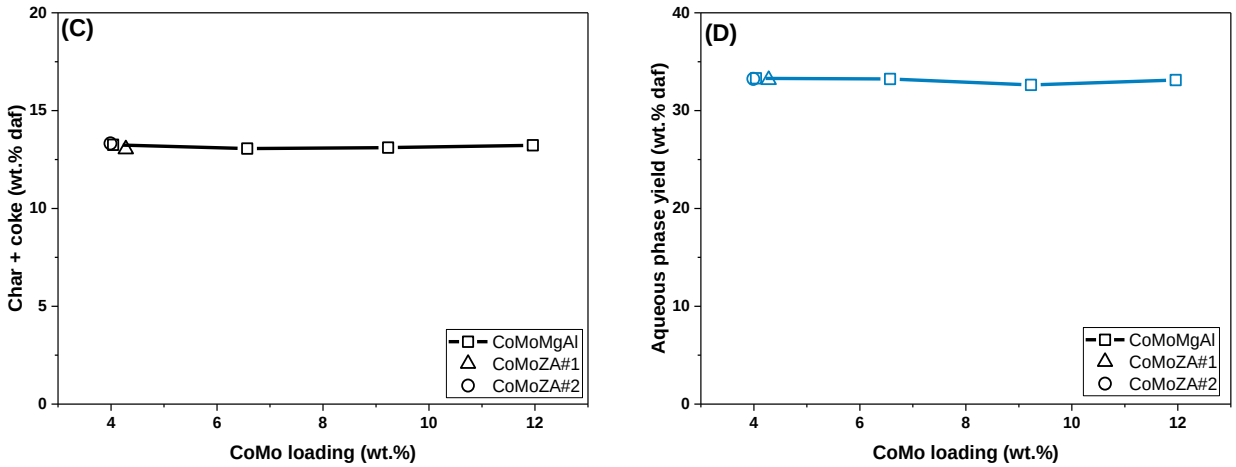

Figure 2 Effect of CoMo loading and support on the condensable organics yield (A), gas yield (B), solid yield (C), and aqueous phase yield (D). Conditions: Fluid bed temperature: 450-455°C, total pressure: 26 bar, biomass feeding rate: 270-282 g/h, feed time: 2.5-3.5 h, H_2 flow: 82 NL/min, N_2 flow: 5 NL/min, and H_2S conc: 460 ppm.

Figure 3(A) shows the CO and CO_2 yield and indicates that the CO_2 yield decreases with increasing CoMo loading. The CO_2 yield was 9.2 wt.% daf when the CoMo loading was 4.1 wt.%, which decreased to 7.7 wt.% daf when the CoMo loading was increased to 12.0 wt.%. Furthermore, increasing the CoMo loading from 4.1 to 9.22 wt.% increased the CO yield from 7.6 to 8.9 wt.% daf, but further increasing the CoMo loading did not increase the CO yield. These results indicate that the catalysts reversed water-gas shift (R.1) and reforming (R.2) activities increase with increasing CoMo loading, thus the CO/CO_2 ratio approaches equilibrium (see supplementary information Figure S.1). However, it could also be due to changes in the catalysts decarbonylation and decarboxylation activity. Using CoMoZA#2 instead of CoMoMgAl#1 decreased the CO_2 yield from 9.2 to 8.4 wt.% daf and increased the CO yield from 6.5 to 7.7 wt.% daf. Interestingly, the CO_2 yield decreased to 7.8 wt.% daf when the CoMoZA#1 was used, but the CO yield only increased to from 6.5 to 6.7 wt.% daf. This indicates that the change in the support alters the catalysts decarbonylation and/or decarboxylation activity and the CO/CO_2 ratio increases and approaches equilibrium with increasing support acidity (CoMoZA#2).

$$CO_2 + H_2 \rightleftharpoons CO + H_2O \quad \text{(R.1)}$$

$$CH_4 + H_2O \rightleftharpoons CO + H_2 \quad \text{(R.2)}$$

Increasing the CoMo loading from 4.1 wt.% to 12.0 wt.% daf decreased the olefin yield from 3.6 to 2.1 wt.% daf and the paraffin yield increased from 3.2 to 5.9 wt.% (see Figure 3 B), thus showing an increase in the hydrogenation activity. Using CoMoZA#1 and CoMoZA#2 instead of CoMoMgAl#1 increased both the C_2-C_3 olefin and paraffin yield. The paraffin yield increased to 5.8 wt.% daf for CoMoZA#1 and 6.0 wt.% daf for CoMoZA#2 and the olefin yield increased to 4.2 wt.% daf for CoMoZA#1 and 4.6 wt.% daf for CoMoZA#2. Furthermore the observed increase in the total C_1-C_3 yield, shown in Figure 2(B), is due to the increase in the C_2-C_3 yield, while the methane yield decreased from 3.5 wt.% for CoMoMgAl#1 to 2.9 wt.% daf for CoMoZA#1 and 3.3 wt.% daf for CoMoZA#2. It is therefore likely that the increased C_2-C_3 paraffin and olefin yield is due to an increased cracking and hydrocracking activity for the CoMoZA#1 and CoMoZA#2 compared to CoMoMgAl#1, which can be ascribed to their higher acidity.

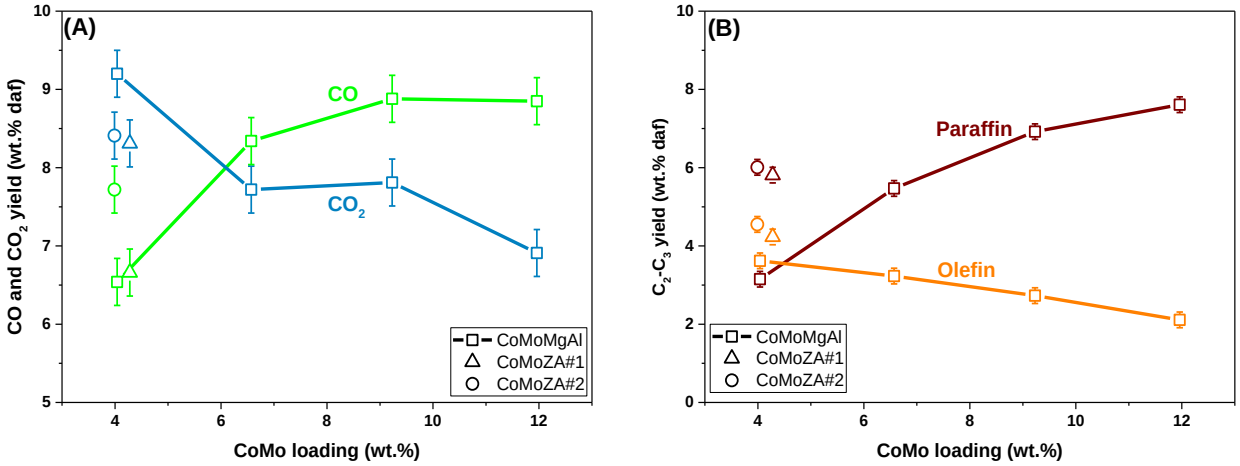

Figure 3 Effect of CoMo loading and support on the CO and CO_2 yield (A) and C_2-C_3 paraffin and olefin yield (B). Conditions: Fluid bed temperature: 450-455°C, total pressure: 26 bar, biomass feeding rate: 270-282 g/h, feed time: 2.5-3.5 h, H_2 flow: 82 NL/min, N_2 flow: 5 NL/min, and H_2S conc: 460 ppm.

3.2 Chemical composition of the condensed liquids

3.2.1 Organic phase

3.2.1.1 Oxygen and hydrogen content

The oxygen and hydrogen content in the condensed organics are shown in Figure 4. As the CoMo loading is increased from 4.1 to 12.0 wt.% for the $MgAl_2O_4$ support the oxygen content decreased from 9.0 to 4.7 wt.% db and the hydrogen content increased from 9.39 to 9.70 wt.% db, showing that the deoxygenation and hydrogenation activity increased with increasing CoMo loading, as expected. Using CoMoZA#1 and

CoMoZA#2 also decreased the oxygen content in the condensed organics, thus the oxygen content was 5.2 wt.% db for CoMoZA#1 and 6.1 wt.% db for CoMoZA#2. The increased deoxygenation activity cannot be explained with an increased decarboxylation and/or decarbonylation activity, since the total CO and CO_2 yield did not increase, indicating that the ZA#1 and ZA#2 supports have a promoting effect on the hydrodeoxygenation activity. Using CoMoZA#1 and CoMoZA#2 also decreased the hydrogen content from 9.39 wt.% db when using CoMoMgAl#1 to 9.30 and 8.99 wt.% db, respectively, indicating a decrease in the hydrogenation activity. As shown in Table 3 increasing the CoMo loading from 4.1 wt.% to 12.0 wt.% also decreased the density of the condensed organics from 0.943 to 0.936 g/ml, which was probably due to the decreased oxygen content. However, the density increased from 0.943 g/ml when using CoMoMgAl#1 to 0.952 and 0.968 g/ml when using CoMoZA#1 and CoMoZA#2, respectively. The TAN for the condensed organics, when CoMoMgAl#1 was used, was 4.00 mg_{KOH}/g, which decreased to 0.30 mg_{KOH}/g when the CoMo loading was increased to 12.0 wt.% and 0.60 when ZA#2 was used as support (see Table 3). This shows that both increasing the support acidity and the metal loading efficiently removes the acid in the condensed organics, which minimizes the risk of corrosion when storing the product.

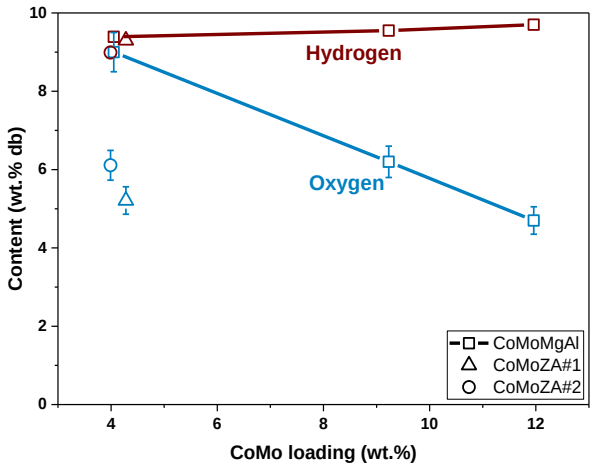

Figure 4 Effect of CoMo loading and support on the oxygen and hydrogen content in the condensed organics. Conditions: Fluid bed temperature: 450-455°C, total pressure: 26 bar, biomass feeding rate: 270-282 g/h, feed time: 2.5-3.5 h, H_2 flow: 82 NL/min, N_2 flow: 5 NL/min, and H_2S conc: 460 ppm.

3.2.1.2 GC×GC-MS/FID

The condensed organic phases were also analyzed with GC×GC-MS/FID. The detected components were divided into the following groups: naphthenes, monoaromatics, diaromatics, triaromatics, larger aromatics, phenols, dihydroxybenzenes, larger oxygenated aromatics, oxygenated aliphatics, paraffins, and sterols. The concentration of paraffins was between 0.46 and 2.2 % area-FID, see supplementary information Figure S.2. The concentration of tri-and larger aromatics varied between 5.9 and 3.9 % area-FID and decreased with the increasing CoMo loading. Changing the support did not significantly change the concentration of tri-and larger aromatics, thus the concentration was 5.2 % area-FID when CoMoMgAl#1 was used and 5.9 and 5.4 % area-FID when CoMoZA#1 and CoMoZA#2 were used, respectively. The concentration of dihydroxybenzenes was between 1.0 and 2.4 % area-FID and decreased with increasing CoMo loading. Traces of sterols (<0.2 % area-FID) were found in all the analyzed organic phases.

Figure 5A shows the concentration of the naphthenes, monoaromatics and diaromatics. As the CoMo loading was increased from 4.1 to 12.0 wt.% the concentration of monoaromatics increased from 8.3 to 27.1 % area-FID, the concentration of diaromatics was constant between 10.6 and 12.1 % area-FID, and the concentration of naphthenes increased from 8.0 to 15.3 % area-FID. The increase in the concentration of naphthenes was probably due to the increased hydrogenation activity when the CoMo loading was increased. Using the zeolite based supports increased the monoaromatic concentration from 8.3 % area-FID with CoMoMgAl#1 to 19.0 and 27.7 % area-FID for CoMoZA#1 and CoMoZA#2, respectively. Only a small change in the concentration of naphthenes was observed, which was 8.0 % area-FID for CoMoMgAl#1, 8.2 % area-FID for CoMoZA#1 and 5.7 % area-FID for CoMoZA#2, hence not correlated to the amount of zeolite in the support. The concentration of diaromatics also increased from 10.6 % area-FID for CoMoMgAl#1 to 22.1 and 17.4 area-FID for CoMoZA#1 and CoMoZA#2, respectively.

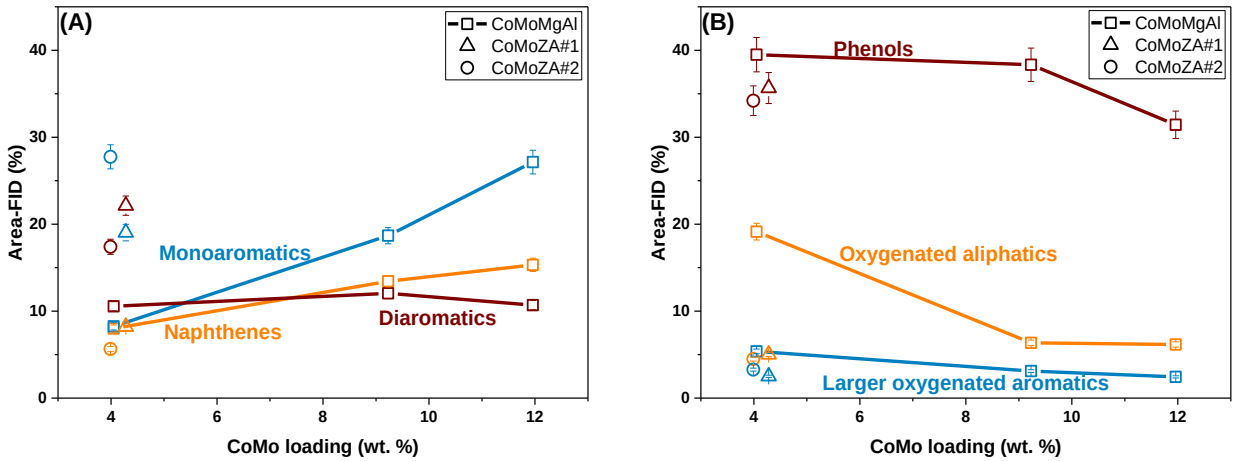

Figure 5 Effect of CoMo loading and support on the concentration of naphthenes, monoaromatics, and diaromatics (A) and the concentration of oxygenated aliphatics, phenols, and larger oxygenated aromatics (B). Conditions: Fluid bed temperature: 450-455°C, total pressure: 26 bar, biomass feeding rate: 270-282 g/h, feed time: 2.5-3.5 h, H_2 flow: 82 NL/min, N_2 flow: 5 NL/min, and H_2S conc: 460 ppm.

The concentration of phenols decreased from 39.5 to 38.3 % area-FID when the CoMo loading was increased from 4.1 to 9.2 wt.%, but decreased to 31.4 % area-FID when the loading was increased to 12.0 wt.%. The concentration of oxygenated aliphatics decreased from 19.1 to 6.3 % area-FID when the CoMo loading was increased from 4.1 to 9.2 wt.%, but further increasing the loading to 12.0 wt.% only decreased the concentration to 6.2 % area-FID, thus the difference was within the uncertainty. The concentration of larger oxygenates decreased with the CoMo loading from 5.4 % area-FID at 4.1 wt.% to 2.4 area-FID at 12.0 wt.%. Overall, this indicates that the oxygenates are easily removed when the CoMo loading is increased, while more activity is needed to remove the phenols. The decrease in the concentration of phenols is not enough to explain the increased concentration of monoaromatics and naphthenes, thus it is very likely that some of the oxygenated aliphatics have participated in alkylation reactions with the aromatics, thus increasing the monoaromatic yield. Similarly Lai et al. [51] observed alkylation reactions when upgrading catalytic hydropyrolysis vapors in a fluid bed reactor.

The concentration of oxygenated aliphatics decreased from 19.1 % area-FID for the CoMoMgAl#1 to 5.0 and 4.5 % area-FID for CoMoZA#1 and CoMoZA#2, respectively. The phenol concentration decreased from 39.5 % area-FID to 35.7 % area-FID when the CoMoZA#1 was used instead of CoMoMgAl#1 and using CoMoZA#2 decreased the concentration to 34.2 % area-FID, thus indicating a similar deoxygenation activity for

CoMoZA#1 and CoMoZA#2. Overall, the zeolite supported catalysts increased the aromatic yield both by deoxygenation of the phenols, but also by enhancing alkylation reactions. Furthermore, the increase in selectivity for monoaromatics with increasing zeolite loading was likely due to the enhanced alkylation.

3.2.1.3 Sulfur specific GC-AED

The condensed organics from the experiment with the CoMoMgAl#1, CoMoMgAl#3, CoMoMgAl#4, and CoMoZA#2 were analyzed with sulfur specific GC-AED. Lists of the detected S containing hydrocarbons can be found in supplementary information Tables S.2-S.6. The samples contained between 185 and 970 wt-ppm organic S, which was divided into five groups: thiols, thiophenes, benzothiophenes, other (methylethylsulfide, dimethylsulfide, carbonylsulfide, dihexyldisulfide), and unidentified as shown in Figure 6. Increasing the CoMo loading from 4.1 to 9.2 wt.% decreased the thiol concentration from 55 to 11 wt-ppm S, which was probably due to a lower concentration of olefins, which otherwise can be converted into thiols through recombination reactions [52–55]. Interestingly, increasing the CoMo loading also increased the concentration of thiophenes from 80 to 250 wt-ppm S and the concentration of benzothiophenes from 29 to 71 wt-ppm S. However, the concentration of unidentified sulfur containing molecules decreased from 501 to 268 wt-ppm, thus the concentration of organic bound sulfur decreased from 823 to 766 wt-ppm S. Further increasing the CoMo loading to 12.0 wt.% decreased the organic sulfur concentration to 545 wt-ppm S, showing that increasing the CoMo loading decreases the sulfur concentration. The reason for the increase in the concentration of thiophenes and benzothiophenes, when the CoMo loading is increased, is possibly because a larger fraction of the sulfur containing molecules was identified (see Figure 6). Unidentified sulfur containing molecules might be substituted thiophenes and benzothiophenes.

Increasing the fraction of H-ZSM-5 in the support increased the concentration of thiophenes, hence it was 80 wt-ppm S when CoMoMgAl#1 was used, 341 wt-ppm S when CoMoZA#1 was used, and 605 wt-ppm S when CoMoZA#2 was used. The total concentration of organic bound sulfur increased from 823 wt-ppm S for the CoMoMgAl#1, to 1121 wt-ppm S for CoMoZA#1, and to 1060 wt-ppm S for the CoMoZA#2, thus H-ZSM-5 increases the amount of sulfur incorporated into the organics. Since formation of thiophenes occurs in fluid

catalytic cracking units where zeolite catalysts are used, it is assumed that the incorporation of sulfur in catalytic hydropyrolysis takes place through similar reaction mechanisms as in an FCC unit [56,57].

This indicates that while having a higher support acidity reduced the oxygen content in the condensed organic phase, it increased the sulfur content, which needs to be removed before it can be used as transportation fuel in the US and EU [58,59]. Dibenzothiophenes, which are known for being very difficult to remove from diesel [60], were not detected in the any of the organic phases, indicating that the sulfur can be removed simultaneously with the removal of the remaining oxygen.

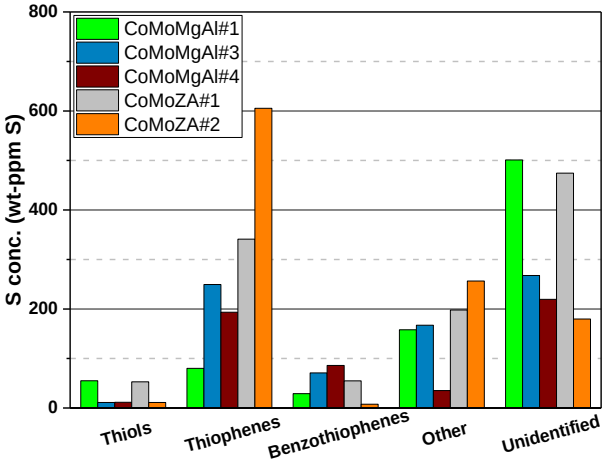

Figure 6 Concentration of sulfur species in the condensed organic phases from experiments with the CoMoMgAl#1, CoMoMgAl#3, CoMoMgAl#4, CoMoZA#1, and CoMoZA#2 catalyst analyzed with S specific GC-AED. Conditions: Fluid bed temperature: 450-455°C, total pressure: 26 bar, biomass feeding rate: 270-282 g/h, feed time: 2.5-3.5 h, H_2 flow: 82 NL/min, N_2 flow: 5 NL/min, and H_2S conc: 460 ppm.

3.2.2 Aqueous phase

Carbon specific GC-AED was used to determine the carbon recovery in the aqueous phases and is shown in Figure 7(A). Increasing the CoMo loading from 4.1 to 9.2 wt.% for the $MgAl_2O_4$ support decreased the carbon recovery in the aqueous phase from 3.2 to 1.1 %, further increasing the CoMo loading to 12.0 wt.% decreased the carbon recovery to 0.97 %, thus as the CoMo loading is increased its impact on the carbon recovery in the aqueous phase decreased. Changing the support material decreased the carbon recovery in the aqueous phase from 3.2 % for CoMoMgAl#1 to 0.67 % for CoMoZA#1 and 0.97 % for CoMoZA#2.

The aqueous phase was also analyzed with GC-MS/FID and the detected molecules were divided into 6 groups: alcohols, furans, acids, phenols, ketones and unidentified as shown in Figure 7(B) and detailed lists of the detected species in the aqueous phases are shown in supplementary information Table S.7-S.11. Increasing the CoMo loading from 4.1 to 12.0 wt.% decreased the concentration of alcohols from 68.5 to 35.8 % area-FID and decreased the concentration of ketones from 19.1 to 7.6 % area-FID, while the phenol concentration increased from 6.7 to 47.1 % area-FID. The increased relative concentration of phenols when the CoMo loading was increased was due to the decreased concentration of alcohols and ketones and decreased carbon in the aqueous phase overall. The concentration of acids increased from 3.8 to 5.5 % area-FID when the CoMo loading was increased from 4.1 to 12.0 wt.%. However, because of the concurrent decrease in the carbon recovery in the aqueous phase the total amount of acids decreased. Varying the support material also lead to a decrease in the concentration of alcohols, thus the concentration was 68.5 % area-FID when the CoMoMgAl#1 was used, but 21.1 and 16.1 % area-FID when the CoMoZA#1 and CoMoZA#2 were used, respectively. This supports the observation for the organic phase that the zeolite supported catalysts removes the oxygenated aliphatics. The relative concentration of phenols increased from 6.7 % area-FID to 48.8 % area-FID for CoMoZA#1 and 59.1 % area-FID for CoMoZA#2. The relative concentration of acids increased from 3.8 % area-FID for CoMoMgAl#1 to 5.5 % area-FID for CoMoZA#1 and 5.6 % area-FID for CoMoZA#2. The relative concentration of ketones was close to constant at 19.1 % area-FID for CoMoMgAl#1, 20.0 % area-FID for CoMoZA#1, and 17.8 % area-FID for CoMoZA#2. Furans were only detected in the aqueous phase from the experiment with CoMoMgAl#1 (0.43 % area-FID) and CoMoZA#1 (0.54 % area-FID). These results therefore show that both increasing the CoMo loading and support acidity leads to an increased relative concentration of phenols in the aqueous phase, due to deoxygenation of the oxygenated aliphatics. The main difference between increasing the CoMo loading and support acidity is that increasing the CoMo loading leads to both a decrease in the alcohols and ketones, while increasing the support acidity only decreases the relative concentration of alcohols. This is most likely because having a higher support acidity increases the degree of alkylation, as previously discussed in section 3.2.1.2.

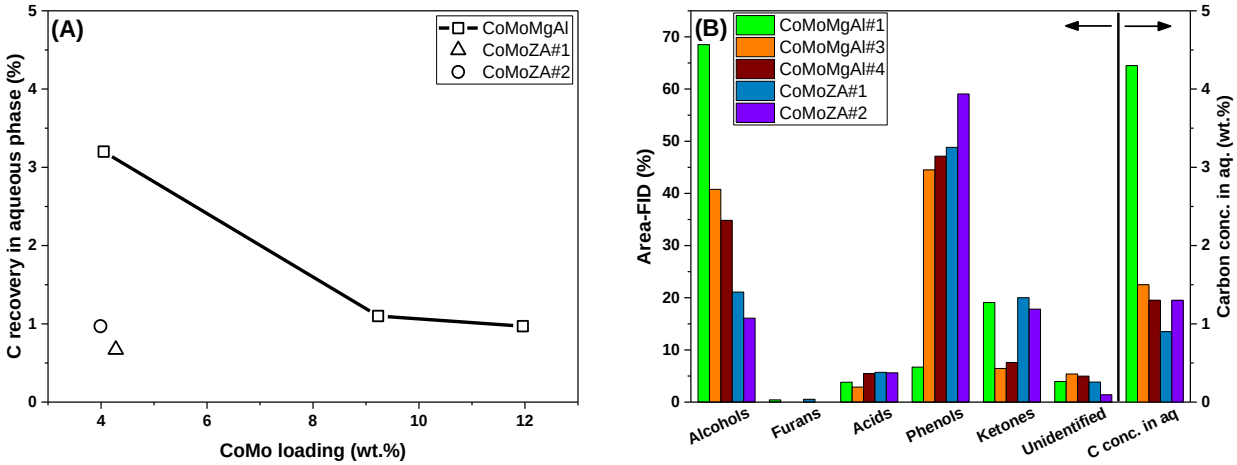

Figure 7 Effect of CoMo loading and support on carbon recovery in the aqueous phase (A) and the composition of the aqueous phase (B). Conditions: Fluid bed temperature: 450-455°C, total pressure: 26 bar, biomass feeding rate: 270-282 g/h, feed time: 2.5-3.5 h, H_2 flow: 82 NL/min, N_2 flow: 5 NL/min, and H_2S conc: 460 ppm.

3.3 Characterization of catalysts

3.3.1 Characterization of catalyst oxide precursors

3.3.1.1 NH_3-TPD

The acidity of the fresh oxide precursors was investigated with NH_3-TPD, as shown in Figure 8. For CoMoMgAl#1 – CoMoMgAl#4 the number of acidic sites increased with increasing surface area (see Figure S.3), as expected. Furthermore, the desorption rate peaks at 255 °C for CoMoMgAl#1 and at 270 °C for CoMoMgAl#4, thus the desorption rate peaks at a higher temperature when the surface area is increased, indicating that the acid strength increases when the calcination temperature is decreased and/or the CoMo loading is increased.

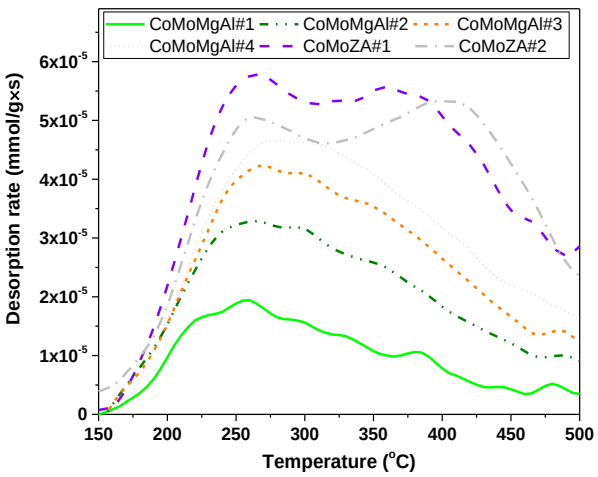

Figure 8 NH_3-TPD profiles for the oxide catalyst precursors

The two zeolite based catalyst precursors CoMoZA#1 and CoMoZA#2 both have a larger number of acidic sites than the $MgAl_2O_4$ based catalysts, which can be seen by both the higher desorption rate in Figure 8 and the higher amount of NH_3 adsorbed and desorbed as shown in Table 4. A substantial difference between the desorption curve of the MgAl supported catalysts and ZA supported catalysts is that the MgAl supported catalysts only have one peak around 260°C, while ZA catalysts have two around 260 °C and 360-410 °C. For the ZA catalysts the first peak is probably mainly due to desorption of NH_3 from the alumina, while the second peak is mainly due to desorption from the zeolite. Interestingly, the amount of NH_3 adsorbed is 0.564 mmol/g for the CoMoZA#1 and 0.529 mmol/g for the CoMoZA#2, indicating that there are more acidic sites on CoMoZA#1 than CoMoZA#2, thus the alumina contains more acidic sites than the zeolite. However, the second desorption peak on CoMoZA#1 is at 360 °C while it is at 410 °C for CoMoZA#2, showing that CoMoZA#2 has stronger acid sites than CoMoZA#1.

Table 4 Concentration of acidic sites (NH_3-TPD) for the oxide catalyst precursors

	CoMoMgAl#1	CoMoMgAl#2	CoMoMgAl#3	CoMoMgAl#4	CoMoZA#1	CoMoZA#2
NH_3 adsorbed (mmol/g)	0.127	0.259	0.333	0.378	0.564	0.529
NH_3 desorbed (mmol/g)	0.124	0.251	0.323	0.374	0.516	0.494

3.3.1.2 Raman spectroscopy

The phases present in the calcined oxide precursors were determined using Raman spectroscopy, as shown in Figure 9. Three or four spectra were measured at different spots for each sample, see supplementary information Figure S.4, which showed a slight variation between different spots for the same catalyst, indicating some phase heterogeneity. For CoMoMgAl#1 the bands observed at 407, 678, and 771 cm^{-1} were ascribed to the $MgAl_2O_4$ spinel support [61]. The intensity of these bands decreased with increasing CoMo loading. This was probably due to lower $MgAl_2O_4$ surface concentration and darkening of the sample. In addition, as the calcination temperature was decreased with increasing CoMo loading (to adjust the surface area) the crystallization of the spinel phase was less developed (see supplementary information Figure S.5). For CoMoZA#1 and CoMoZA#2 the bands at 301, 373, 470, and 828 cm^{-1} were ascribed to H-ZSM-5, while the bands at 565 and 670 cm^{-1} were ascribed to Al_2O_3.

393 Crystalline MoO_3 has a sharp peak at 992 cm^{-1} due to terminal Mo=O stretching [62], a phase which can
394 therefore be ruled out. The broad band at 920-950 cm^{-1} observed for all the $MgAl_2O_4$ supported samples
395 corresponds to a Mo-O distance of approximately 1.7 Å, which is related to terminal Mo=O units. In the
396 presence of ambient humidity, dispersed MoO_x surface species can get rehydrated and form mixtures of
397 MoO_4^{2-} (aq) (isolated, tetrahedral), $Mo_7O_{24}^{6-}$ and $Mo_8O_{26}^{4-}$ (aq) depending on the acid-base properties of the
398 support [63]. Therefore, the observed band at 320-340 cm^{-1} is assigned to distorted MoO_4^{2-} species [63],
399 which also contributes at 837 and 897 cm^{-1}. Furthermore $Mo_7O_{24}^{6-}$ contributes at 210, 270, 362, 903, and 943
400 cm^{-1}, while $Mo_8O_{26}^{4-}$ at 230, 370, 590, 925, 965 cm^{-1} [62,63]. The intensity of the band at 595 cm^{-1} increased
401 with increasing CoMo loading, indicating that more $Mo_8O_{26}^{4-}$ is formed at high loadings, which is probably
402 related to the slightly higher surface acidity of the support. The sharp peaks at 370 cm^{-1} and 879 cm^{-1} (only
403 observed for CoMoMgAl#1) can be assigned to hydrated $CoMoO_4$ and would represent a Mo-O distance of
404 1.75 Å [64] which is most likely a Mo-O-X (X=support or active metal) entity. The presence of a sharp doublet
405 at 940-950 cm^{-1} is only observed for CoMoMgAl#1 and ascribed to β-CoMoO4 [65]. It should be noted that
406 the hydrated $CoMoO_4 \cdot xH_2O$ phase has a small band at ~870 cm^{-1} together with a broad band at ~930 cm^{-1}
407 [65], which reflects that the metal coordination for $CoMoO_4 \cdot xH_2O$ and β-$CoMoO_4$ are very similar, both
408 containing CoO_6 octahdra and MoO_4 tetrahedra [66]. It is noted that the small band at ~870 cm^{-1} decreases
409 with increasing metal loading. Co_3O_4 would have its main contribution at 692 cm^{-1}, which is not observed,
410 thus indicating that Co is mainly located as hydrated $CoMoO_4$. A monolayer coverage of Mo on Al_2O_3
411 corresponds to 4.5 Mo atoms/nm^2 [62]. Assuming an even distribution of CoMo on the support, the $MgAl_2O_4$
412 supported samples exhibits a monolayer coverage of approximately 73-104 %, thus interactions between the
413 molybdenum species are expected and true isolated sites are unlikely. However, assuming an even
414 distribution on the H-ZSM-5 and Al_2O_3 the coverage for CoMoZA#1 and CoMoZA#2 was 16 and 13 %,
415 respectively, which makes isolated sites more likely. On the other hand, as discussed in section 3.3.2.2, the
416 CoMo was mainly located on the Al_2O_3, thus the coverage was higher on the Al_2O_3 compared to H-ZSM-5.
417 Furthermore, the blue shift of the Mo=O related bands toward 975 cm^{-1} for the zeolite containing supports

418 is likely related to a higher degree of polymerization of the surface Mo-species (as e.g. β-$Mo_8O_{26}^{4-}$), an effect
419 of the increasing surface acidity of the support [67].

420 Overall, the Raman spectra showed that the Co and Mo species formed on the $MgAl_2O_4$ supported catalysts
421 were similar and mainly related to $CoMoO_4$ phases. This was the purpose of adjusting the total surface area
422 and maintaining approximately constant Mo/nm^2 surface loading and Co/Mo ratio when changing the total
423 metal loading. The two ZA supported catalysts also showed similar Mo and Co species, which were mainly
424 present as dispersed polyoxometalates like β-$Mo_8O_{26}^{4-}$.

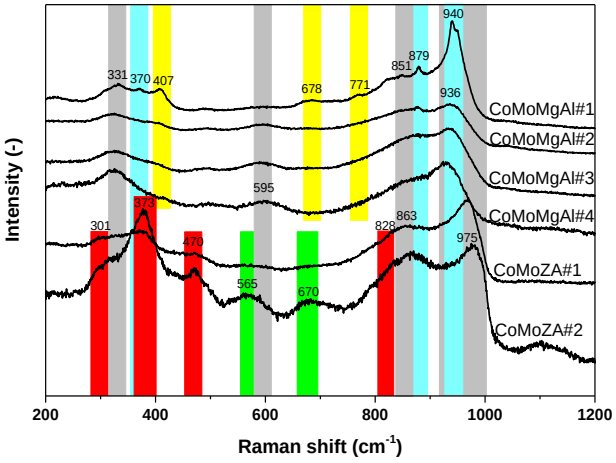

425

426 **Figure 9 Raman spectra of oxide catalyst precursors (calcined, not dehydrated). The Raman bands were assigned to hydrated MoO_x**
427 **(gray), hydrated $CoMoO_4$ (blue), $MgAl_2O_4$ (yellow), H-ZSM-5 (red), and Al_2O_3 (green).**

428 ### 3.3.2 Characterization of the spent catalysts

429 #### *3.3.2.1 SEM-EDS*

430 The catalysts were analyzed with SEM combined with EDS to quantify the carbon and potassium content. The
431 carbon and potassium content of both the fresh and spent catalysts were measured at 3, 5, 10 and 15 kV. At
432 3 kV the concentration near the surface was measured, while at 15 kV a larger volume towards the bulk was
433 measured integrating the signals from both the surface and bulk. However, even at 15 kV the expected
434 penetration depth is only 1.7 µm, as described in [44]. The measured carbon and potassium concentration
435 on the fresh and spent catalysts are shown in supplementary information Table S.12. Since the sample is
436 placed on carbon tape it is assumed that this gives an offset for the carbon measurement, however this is

accounted for by subtracting the carbon content measured on the fresh catalyst (placed on the same tape) from the content measured on the spent catalyst.

Figure 10(A) shows the carbon content (measured at 15 kV) per square meter surface area of the corresponding fresh catalyst. The relative carbon content on the spent catalysts increased from 0.25 mg_{carbon}/m^2 to 0.92 mg_{carbon}/m^2 when the surface area increased from 60 to 148 m^2/g. Part of the reason for the increasing carbon content is that the number of acidic sites and the acid strength of the fresh oxide precursor increased with increasing surface area (see Figure 8 and Table 4). de Jong et al. [68] investigated coking of MoS_2/Al_2O_3 catalysts during hydroprocessing of vacuum gas oil and observed an increase in the degree of coking when the Mo loading was increased. The increase was most likely because the Brønsted sites on MoS_2 promote the formation of coke through the formation of carbonium cations as intermediates [69]. Therefore, the increased loading, and thus increased Brønsted acidity, has most likely increased the carbon content on the spent catalyst in this work. The carbon content on the spent CoMoZA#1 and CoMoZA#2 was 0.11 and 0.092 mg_{carbon}/m^2, hence significantly lower than for CoMoMgAl#1 (0.25 mg_{carbon}/m^2). This is probably because the micro pores in the zeolites are too narrow for the larger aromatics to enter. Despite that the carbon content per square meter decreased, the total carbon content ($mg_{carbon}/g_{catalyst}$) on the spent CoMoZA#1 and CoMoZA#2 did increase compared to CoMoMgAl#1 (see supplementary information Figure S.6).

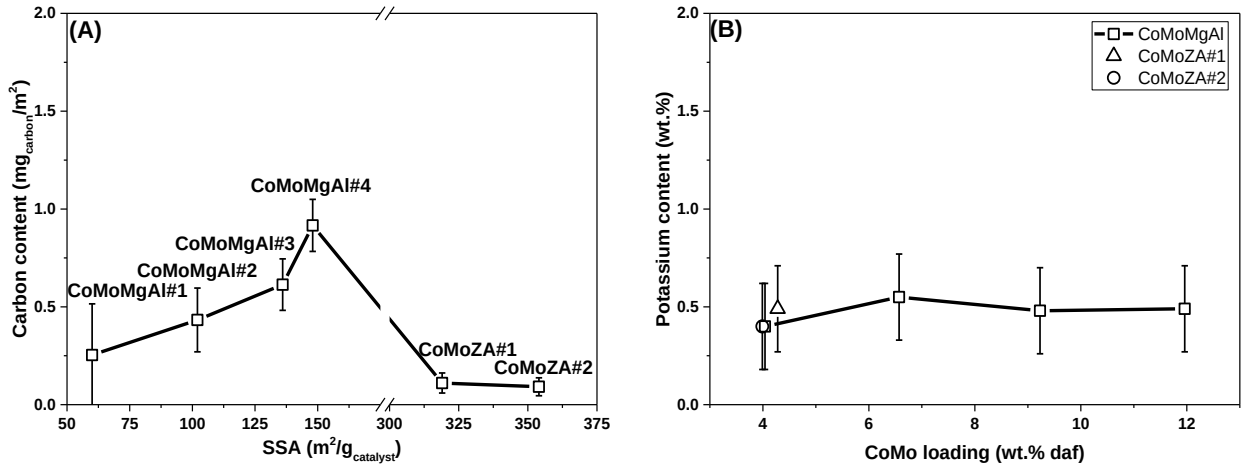

Figure 10 Effect of CoMo loading and support on the carbon content (A) and the potassium content measured at 15 kV (B) on the spent catalysts. Conditions: Fluid bed temperature: 450-455°C, total pressure: 26 bar, biomass feeding rate: 270-282 g/h, feed time: 2.5-3.5 h, H_2 flow: 82 NL/min, N_2 flow: 5 NL/min, and H_2S conc: 460 ppm.

The potassium content on the spent catalysts varied between 0.40 and 0.55 wt.% (see Figure 10(B)), which was within the uncertainty of the measurement. It is well-known that that potassium can decrease the number of Brønsted acid sites [70–74], which decreases the HDO activity of sulfided NiMo catalysts [55], hence catalyst deactivation due to potassium transferred from the biomass could be a serious problem. Since the catalyst saturation level, at which potassium does no longer diffuses into the catalyst, is likely correlated with the number of Brønsted sites [70], significantly more potassium can potentially be transferred to the zeolite based catalysts, CoMoZA#1 and CoMoZA#2. However, since there is no significant difference in the potassium level of the spent catalyst, this indicates that the catalysts are not saturated with potassium and the content of potassium was limited by the transfer from the biomass to the catalyst. This is expected since the total amount of biomass used per catalyst mass was also relatively low in these experiments. Thus, the advantage of using zeolite based supports might decrease when the process is up-scaled, because they will lose their acidity over time.

3.3.2.2 HAADF-STEM

The spent catalysts were also characterized with HAADF-STEM and an image of the spent CoMoMgAl#3 is shown in Figure 11(A). This shows nanometer sized slab structures with bright contrast, which are well-dispersed on the surface of the support grains. An example of a two-layer slab structure is indicated in the figure, where the interlayer distance of 0.62 nm is in accordance with the MoS_2 (002) crystal planes. Therefore the bright-contrasted slabs are ascribed to MoS_2 nanocrystals observed with the (001) basal plane along the direction of the electron beam and located with the basal-plane on the surface of the $MgAl_2O_4$, as previously reported [75]. The slab lengths for the spent catalysts were measured from the STEM images (173-199 slabs per sample) and fitted with a log-normal distribution as shown in Figure 11(B). The slab length distribution was narrower for the zeolite mixed with alumina supported catalysts compared to the catalysts supported on $MgAl_2O_4$. The mean slab length was 1.96 nm for CoMoZA#1 and 2.25 nm for CoMoZA#2, while it was

between 2.65 and 3.07 nm for the catalysts supported on $MgAl_2O_4$. The frequency of monolayer slabs was between 94 and 99 % for all the catalysts, as shown in Figure 11(C), indicating a fairly similar degree of stacking and that most of the active sites were of the Type I structure [47]. The difference in slab length is most likely due to a lower Mo loading on the CoMoZA#1 (0.71 atoms/nm^2) and CoMoZA#2 (0.60 atoms/nm^2) compared to the catalysts on $MgAl_2O_4$ (3.3-4.7 atoms/nm^2).

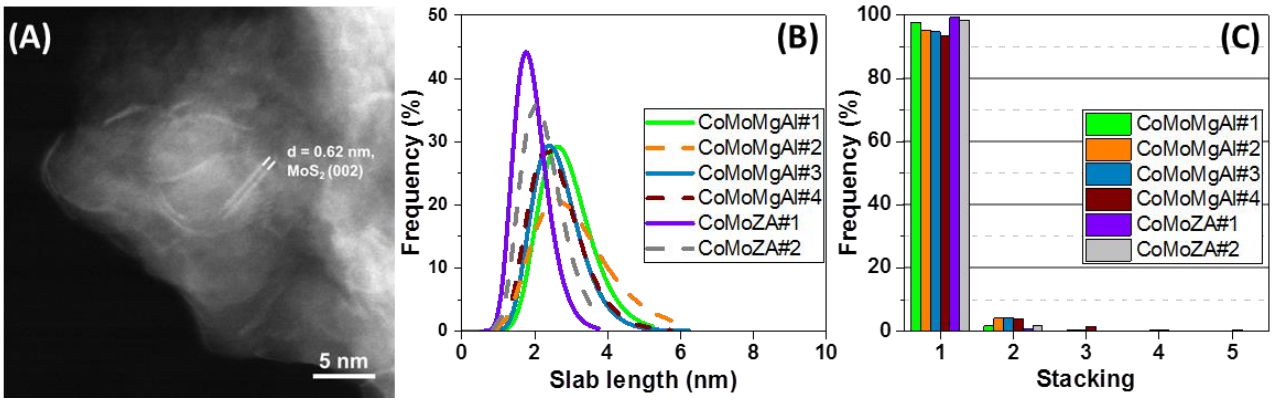

Figure 11 HAADF-STEM image of CoMoMgAl#3 (A), log-normal distribution of the MoS_2 slab lengths for the used catalysts (B), and the degree of MoS_2 stacking (C).

An example of the distribution of cobalt, molybdenum, and sulfur is shown for CoMoZA#2 in Figure 12. The alumina and zeolite phases are clearly discriminated by having a high concentration in aluminum or silicon EDS signals, respectively, see Figure 12 (A). It is observed that a layer of about 50-100 nm alumina is surrounding the zeolite crystals and that the cobalt, molybdenum, and sulfur are well-distributed on the alumina parts of the catalyst. This is consistent with the observed uniformly and well-distributed MoS_2 structures in Figure 11(A), and indicates a successful incorporation of the cobalt into the MoS_2 structure, forming the so-called CoMoS phase [38]. Element maps of the other catalysts also showed the formation of the CoMoS phase (See supplementary information Figures S.7-S.12). The similar slab lengths, degree of stacking and formation of the CoMoS phase shows that the catalysts are representative for comparing the effect of the CoMo loading and the support acidity.

Potassium was also detected on all the samples and it was well-dispersed on the catalysts (See supplementary information Figures S.7-S.12), and in particular found with a high concentration on the zeolite

parts, as indicated in Figure 12 (D), confirming the potassium transfer from the biomass to the catalysts observed with SEM-EDS. Furthermore, it also indicates that the potassium adsorbs on the Brønsted acid sites [70] by ion-exchanging H-ZSM-5 to K-ZSM-5.

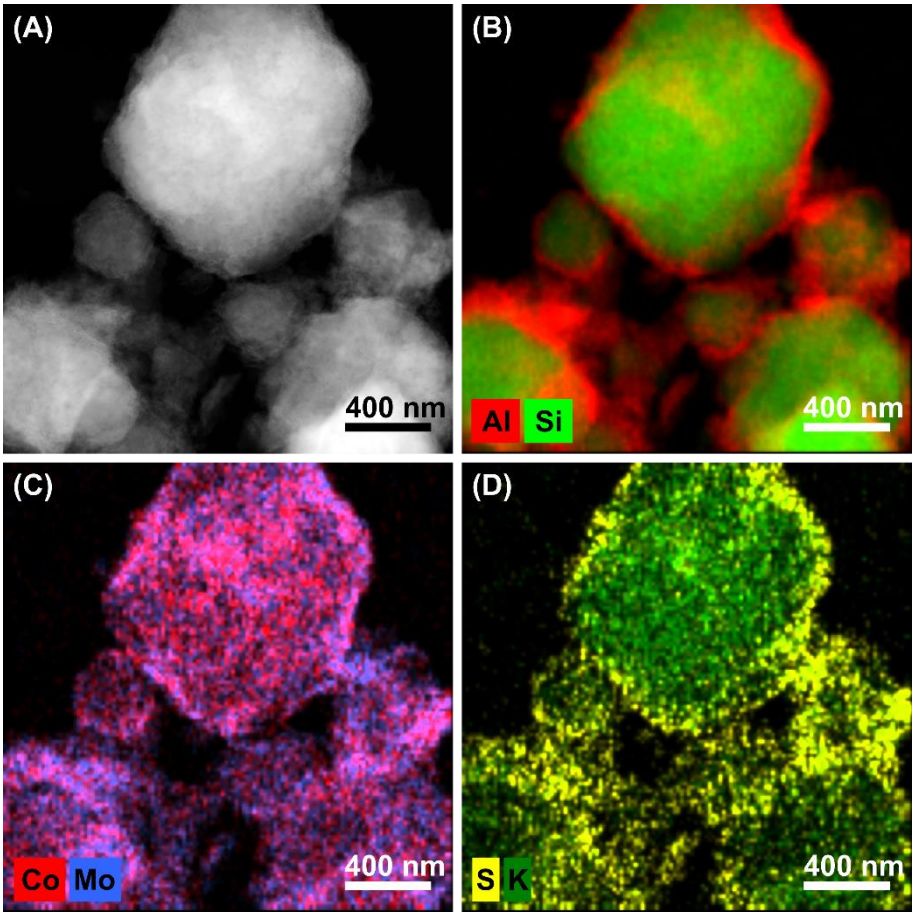

Figure 12 HAADF-STEM image of CoMoZAl#2 (A), EDS element distribution of aluminum and silicon (B) cobalt and molybdenum, (C) and sulfur and potassium (D).

4 Conclusion

Catalytic hydropyrolysis of beech wood in a fluid bed reactor have been studied at 450 °C and 26 bar using different CoMo catalysts. Using $MgAl_2O_4$ as support material the effect of varying the CoMo loading was investigated. Increasing the CoMo loading from 4.1 to 12.0 wt.% decreased the condensable organic yield from 25.2 to 22.7 wt.% and decreased the oxygen content from 9.0 to 4.7 wt.% db. The carbon recovery in the condensable organics (condensed organics and C_{4+} in the gas) decreased from 39 to 37 wt.%, where the

decrease in carbon recovery was most likely due to an increased yield of C_1-C_3 from 10.3 to 14.0 wt.% daf. GC×GC showed that remaining oxygenates in the organic phase were mainly phenols.

The effect of the support acidity was also investigated by testing two CoMo catalysts supported on zeolite (H-ZSM-5) mixed with alumina at different ratios with CoMo loading of 4.1 wt.%. This showed that using zeolite as support increased the hydrocracking and/or cracking activity. Furthermore, it also decreased the oxygen content in organic phase from 9.0 wt.% db to between 5.2 and 6.1 wt.% db, depending on the zeolite content. The results further indicated an increased rate of alkylation reactions when the zeolite based supports were used, as the yield of mono-and diaromatics increased. The carbon recovery in the condensable organics was between 39 and 40 %, showing that the zeolite support can decrease the oxygen content in organic phase without decreasing the carbon recovery. This work therefore shows that it is possible to decrease the oxygen content in the organic phase by increasing the CoMo loading and/or changing the support acidity, while maintaining a high condensable organic yield.

SEM and STEM combined with EDS showed that potassium was transferred from the biomass to the catalysts. Since it is well-known that potassium decreases the number of acidic sites, it is likely that the positive effect of using zeolites will be lost over time. Therefore, further investigations are needed to understand the catalyst deactivation.

5 Acknowledgments

This work is part of the project “Hydrogen assisted catalytic pyrolysis for green fuels” project conducted at The Department of Chemical and Biochemical Engineering at the Technical University of Denmark (DTU). The work was supported by The Danish Council for Strategic Research (now Innovation Fund Denmark, project 1305-00015B), The Programme Commission on Sustainable Energy and Environment. Funding from DTU is also gratefully acknowledged. The authors also acknowledge Aino Nielsen (Haldor Topsøe A/S) for technical assistance with the Raman spectroscopy, Søren Birk Rasmussen for assistance with NH_3-TPD ,the Inorganic

Analysis Department at Haldor Topsøe A/S for technical assistance with the elemental analysis of the fresh oxide precursors by inductive coupled plasma optical emission spectroscopy (IPC-OES) and wavelength dispersive X-ray fluorescence (WD-XRF), and the Organic Analysis Department at Haldor Topsøe A/S for analysis of the organic phase.

6 References

[1] United Nations. Sustainable development goals 2016. http://www.un.org/sustainabledevelopment/energy/ (accessed April 21, 2016).

[2] IPCC - Intergovernmental Panel on Climate Change. Global Warming of 1.5°C an IPCC special report on the impacts of global warming of 1.5 °C above pre-industrial levels and related global greenhouse gas emission pathways, in the context of strengthening the global response to the threat of climate change, 2018.

[3] Independent Statistics & Analysis - U.S. Energy Information Administration. International energy outlook 2016 - DOE/EIA-0484. 2016.

[4] Hansen J, Sato M, Hearty P, Ruedy R, Kelley M, Masson-Delmotte V, et al. Ice melt, sea level rise and superstorms: Evidence from paleoclimate data, climate modeling, and modern observations that 2 °C global warming could be dangerous. Atmos Chem Phys 2016;16:3761–812. https://doi.org/10.5194/acp-16-3761-2016.

[5] Marker TL, Felix LG, Linck MB, Roberts MJ. Integrated hydropyrolysis and hydroconversion (IH^2) for the direct production of gasoline and diesel fuels or blending components from biomass, Part 1: Proof of principle testing. Environ Prog Sustain Energy 2012;31:191–9. https://doi.org/10.1002/ep.10629.

[6] Marker TL, Felix LG, Linck MB, Roberts MJ, Ortiz-Toral P, Wangerow J. Integrated hydropyrolysis and

hydroconversion ($IH^{2®}$) for the direct production of gasoline and diesel fuels or blending components from biomass, Part 2: Continuous testing. Environ Prog Sustain Energy 2014;33:762–8. https://doi.org/10.1002/ep.11906.

[7] Maleche E, Glaser R, Marker T, Shonnard D. A preliminary life cycle assessment of biofuels produced by the $IH^{2\ TM}$ process. Environ Prog Sustain Energy 2014;33:322–9. https://doi.org/10.1002/ep.11773.

[8] Fan J, Gephart J, Marker T, Stover D, Updike B, Shonnard DR. Carbon Footprint Analysis of Gasoline and Diesel from Forest Residues and Corn Stover using Integrated Hydropyrolysis and Hydroconversion. ACS Sustain Chem Eng 2016;4:284–90. https://doi.org/10.1021/acssuschemeng.5b01173.

[9] Winjobi O, Tavakoli H, Klemetsrud B, Handler R, Marker T, Roberts M, et al. Carbon Footprint Analysis of Gasoline and Diesel from Forest Residues and Algae using Integrated Hydropyrolysis and Hydroconversion Plus Fischer–Tropsch (IH 2 Plus cool GTL). ACS Sustain Chem Eng 2018;6:10766–77. https://doi.org/10.1021/acssuschemeng.8b02091.

[10] Nguyen T Van, Clausen LR. Thermodynamic analysis of polygeneration systems based on catalytic hydropyrolysis for the production of bio-oil and fuels. Energy Convers Manag 2018;171:1617–38. https://doi.org/sus10.1016/j.enconman.2018.06.024.

[11] Dayton DC, Carpenter J, Farmer J, Turk B, Gupta R. Biomass hydropyrolysis in a pressurized fluidized bed reactor. Energy & Fuels 2013;27:3778–85. https://doi.org/10.1021/ef400355t.

[12] Dayton DC, Hlebak J, Carpenter JR, Wang K, Mante OD, Peters JE. Biomass hydropyrolysis in a fluidized bed reactor. Energy & Fuels 2016;30:4879–87. https://doi.org/10.1021/acs.energyfuels.6b00373.

579 [13] Wang K, Dayton DC, Peters JE, Mante OD. Reactive catalytic fast pyrolysis of biomass to produce
580 high-quality bio-crude. Green Chem 2017;19:3243–51. https://doi.org/10.1039/C7GC01088E.

581 [14] Gamliel DP, Bollas GM, Valla JA. Two-stage catalytic fast hydropyrolysis of biomass for the
582 production of drop-in biofuel. Fuel 2018;216:160–70. https://doi.org/10.1016/j.fuel.2017.12.017.

583 [15] Gamliel DP, Wilcox L, Valla JA. The effects of catalyst properties on the conversion of biomass via
584 catalytic fast hydropyrolysis. Energy & Fuels 2017;31:679–87.
585 https://doi.org/10.1021/acs.energyfuels.6b02781.

586 [16] Gamliel DP, Bollas GM, Valla JA. Bifunctional Ni-ZSM-5 catalysts for the pyrolysis and hydropyrolysis
587 of biomass. Energy Technol 2017;5:172–82. https://doi.org/10.1002/ente.201600136.

588 [17] Chandler DS, Resende FLP. Comparison between Catalytic Fast Pyrolysis and Catalytic Fast
589 Hydropyrolysis for the Production of Liquid Fuels in a Fluidized Bed Reactor. Energy and Fuels
590 2019;33:3199–209. https://doi.org/10.1021/acs.energyfuels.8b03782.

591 [18] Thangalazhy-Gopakumar S, Adhikari S, Gupta RB, Tu M, Taylor S. Production of hydrocarbon fuels
592 from biomass using catalytic pyrolysis under helium and hydrogen environments. Bioresour Technol
593 2011;102:6742–9. https://doi.org/10.1016/j.biortech.2011.03.104.

594 [19] Thangalazhy-Gopakumar S, Adhikari S, Gupta RB. Catalytic pyrolysis of biomass over H^{+}ZSM-5 under
595 hydrogen pressure. Energy & Fuels 2012;26:5300–6. https://doi.org/10.1021/ef3008213.

596 [20] Jan O, Marchand R, Anjos LCA, Seufitelli GVS, Nikolla E, Resende FLP. Hydropyrolysis of lignin using
597 Pd/HZSM-5. Energy & Fuels 2015;29:1793–800. https://doi.org/10.1021/ef502779s.

598 [21] Melligan F, Hayes MHB, Kwapinski W, Leahy JJ. Hydro-pyrolysis of biomass and online catalytic vapor
599 upgrading with Ni-ZSM-5 and Ni-MCM-41. Energy & Fuels 2012;26:6080–90.
600 https://doi.org/10.1021/ef301244h.

601 [22] Choudhary P, Malik A, Pant KK. Mass-Scale Algal Biomass Production Using Algal Biofilm Reactor and
602 Conversion to Energy and Chemical Precursors by Hydropyrolysis. ACS Sustain Chem Eng
603 2017;5:4234–42. https://doi.org/10.1021/acssuschemeng.7b00233.

604 [23] Pindoria R., Megaritis A, Herod A., Kandiyoti R. A two-stage fixed-bed reactor for direct
605 hydrotreatment of volatiles from the hydropyrolysis of biomass: effect of catalyst temperature,
606 pressure and catalyst ageing time on product characteristics. Fuel 1998;77:1715–26.
607 https://doi.org/10.1016/S0016-2361(98)00079-9.

608 [24] Melligan F, Hayes MHB, Kwapinski W, Leahy JJ. A study of hydrogen pressure during hydropyrolysis
609 of Miscanthus x giganteus and online catalytic vapour upgrading with Ni on ZSM-5. J Anal Appl
610 Pyrolysis 2013;103:369–77. https://doi.org/10.1016/j.jaap.2013.01.005.

611 [25] Dabros TMH, Stummann MZ, Høj M, Jensen PA, Grunwaldt J-D, Gabrielsen J, et al. Transportation
612 fuels from biomass fast pyrolysis, catalytic hydrodeoxygenation, and catalytic fast hydropyrolysis.
613 Prog Energy Combust Sci 2018;68:268–309. https://doi.org/10.1016/j.pecs.2018.05.002.

614 [26] Trinh TN, Jensen PA, Dam-Johansen K, Knudsen NO, Sørensen HR, Hvilsted S. Comparison of lignin,
615 macroalgae, wood, and straw fast pyrolysis. Energy & Fuels 2013;27:1399–409.
616 https://doi.org/10.1021/ef301927y.

617 [27] Şenol Oİ, Viljava T-R, Krause AOI. Hydrodeoxygenation of aliphatic esters on sulphided NiMo/γ-Al_2O_3
618 and CoMo/γ-Al2O3 catalyst: The effect of water. Catal Today 2005;106:186–9.
619 https://doi.org/10.1016/j.cattod.2005.07.129.

620 [28] Şenol OI, Ryymin EM, Viljava TR, Krause AOI. Reactions of methyl heptanoate hydrodeoxygenation
621 on sulphided catalysts. J Mol Catal A Chem 2007;268:1–8.
622 https://doi.org/10.1016/j.molcata.2006.12.006.

623 [29] Şenol Oİ, Viljava T-R, Krause AOI. Effect of sulphiding agents on the hydrodeoxygenation of aliphatic
624 esters on sulphided catalysts. Appl Catal A Gen 2007;326:236–44.
625 https://doi.org/10.1016/j.apcata.2007.04.022.

626 [30] Ryymin E-M, Honkela ML, Viljava T-R, Krause AOI. Competitive reactions and mechanisms in the
627 simultaneous HDO of phenol and methyl heptanoate over sulphided NiMo/γ-Al_2O_3. Appl Catal A Gen
628 2010;389:114–21. https://doi.org/10.1016/j.apcata.2010.09.010.

629 [31] Gutierrez A, Turpeinen E-M, Viljava T-R, Krause O. Hydrodeoxygenation of model compounds on
630 sulfided CoMo/γ-Al2O3 and NiMo/γ-Al2O3 catalysts; Role of sulfur-containing groups in reaction
631 networks. Catal Today 2017;285:125–34. https://doi.org/10.1016/j.cattod.2017.02.003.

632 [32] Dabros TMH, Gaur A, Pintos DG, Sprenger P, Høj M, Hansen TW, et al. Influence of H2O and H2S on
633 the composition, activity, and stability of sulfided Mo, CoMo, and NiMo supported on MgAl2O4 for
634 hydrodeoxygenation of ethylene glycol. Appl Catal A Gen 2018;551:106–21.
635 https://doi.org/10.1016/j.apcata.2017.12.008.

636 [33] Bui VN, Laurenti D, Afanasiev P, Geantet C. Hydrodeoxygenation of guaiacol with CoMo catalysts.
637 Part I: Promoting effect of cobalt on HDO selectivity and activity. Appl Catal B Environ
638 2011;101:239–45. https://doi.org/10.1016/j.apcatb.2010.10.025.

639 [34] Centeno A, Laurent E, Delmon B. Influence of the support of CoMo sulfide catalysts and of the
640 addition of potassium and platinum on the catalytic performances for the hydrodeoxygenation of
641 carbonyl, carboxyl, and guaiacol-type molecules. J Catal 1995;154:288–98.
642 https://doi.org/10.1006/jcat.1995.1170.

643 [35] Badawi M, Paul J-F, Cristol S, Payen E. Guaiacol derivatives and inhibiting species adsorption over
644 MoS_2 and CoMoS catalysts under HDO conditions: A DFT study. Catal Commun 2011;12:901–5.
645 https://doi.org/10.1016/j.catcom.2011.02.010.

[36] Raybaud P, Hafner J, Kresse G, Kasztelan S, Toulhoat H. Structure, energetics, and electronic properties of the surface of a promoted MoS2 catalyst: An ab initio local density functional study. J Catal 2000;190:128–43. https://doi.org/10.1006/jcat.1999.2743.

[37] Leliveld BRG, van Dillen JAJ, Geus JW, Koningsberger DC, de Boer M. Structure and Nature of the Active Sites in CoMo Hydrotreating Catalysts. An EXAFS Study of the Reaction with Selenophene. J Phys Chem B 1997;101:11160–71. https://doi.org/10.1021/jp9723933.

[38] Topsøe H, Clausen BS, Massoth FE. Catalysis - Science and Technology. Hydrotreating catalysis. Volume 11. Berlin Heidelberg, Germany: Springer-Verlag; 1996.

[39] Bouvier C, Romero Y, Richard F, Brunet S. Effect of H_2S and CO on the transformation of 2-ethylphenol as a model compound of bio-crude over sulfided Mo-based catalysts: propositions of promoted active sites for deoxygenation pathways based on an experimental study. Green Chem 2011;13:2441–51. https://doi.org/10.1039/c1gc15181a.

[40] Bui VN, Laurenti D, Delichère P, Geantet C. Hydrodeoxygenation of guaiacol. Part II: Support effect for CoMoS catalysts on HDO activity and selectivity. Appl Catal B Environ 2011;101:246–55. https://doi.org/10.1016/j.apcatb.2010.10.031.

[41] Gonçalves VOO, Brunet S, Richard F. Hydrodeoxygenation of cresols over Mo/Al_2O_3 and $CoMo/Al_2O_3$ sulfided catalysts. Catal Letters 2016;146:1562–73. https://doi.org/10.1007/s10562-016-1787-5.

[42] Schachtl E, Yoo JS, Gutiérrez OY, Studt F, Lercher JA. Impact of Ni promotion on the hydrogenation pathways of phenanthrene on MoS_2/γ-Al_2O_3. J Catal 2017;352:171–81. https://doi.org/10.1016/j.jcat.2017.05.003.

[43] Stummann MZ, Høj M, Schandel CB, Hansen AB, Wiwel P, Gabrielsen J, et al. Hydrogen assisted catalytic biomass pyrolysis. Effect of temperature and pressure. Biomass and Bioenergy

668 2018;115:97–107. https://doi.org/10.1016/j.biombioe.2018.04.012.

669 [44] Stummann MZ, Hansen AB, Hansen LP, Davidsen B, Rasmussen SB, Wiwel P, et al. Catalytic
670 Hydropyrolysis of Biomass Using Molybdenum Sulfide Based Catalyst. Effect of Promoters. Energy &
671 Fuels 2019;33:1302–13. https://doi.org/10.1021/acs.energyfuels.8b04191.

672 [45] Stummann MZ, Høj M, Davidsen B, Hansen AB, Hansen LP, Wiwel P, et al. Effect of the catalyst in
673 fluid bed catalytic hydropyrolysis. Catal Today 2019. https://doi.org/10.1016/j.cattod.2019.01.047.

674 [46] Houssenbay S, Payen E, Kasztelan S, Grimblot J. Oxidic precursors of molybdena supported on nickel
675 and magnesium aluminate hydrotreating catalysts. Catal Today 1991;10:541–60.
676 https://doi.org/10.1016/0920-5861(91)80038-B.

677 [47] Topsøe H. The role of Co-Mo-S type structures in hydrotreating catalysts. Appl Catal A Gen
678 2007;322:3–8. https://doi.org/10.1016/j.apcata.2007.01.002.

679 [48] Wivel C, Candia R, Clausen BS, Mørup S, Topsøe H. On the catalytic significance of a CoMoS phase in
680 CoMo Al2O3hydrodesulfurization catalysts: Combined in situ Mössbauer emission spectroscopy and
681 activity studies. J Catal 1981;68:453–63. https://doi.org/10.1016/0021-9517(81)90115-9.

682 [49] Stummann MZ, Hansen AB, Hansen LP, Davidsen B, Rasmussen SB, Wiwel P, et al. Catalytic
683 Hydropyrolysis of Biomass Using Molybdenum Sulfide Based Catalyst. Effect of Promoters. Energy &
684 Fuels 2019;33:1302–13. https://doi.org/10.1021/acs.energyfuels.8b04191.

685 [50] Beato P, Schachtl E, Barbera K, Bonino F, Bordiga S. Operando Raman spectroscopy applying novel
686 fluidized bed micro-reactor technology. Catal Today 2013;205:128–33.
687 https://doi.org/10.1016/j.cattod.2012.09.030.

688 [51] Lai J, Zhang L, Gong K. Nuclear magnetic resonance characterization of renewable products from a
689 two-step ex-situ hydropyrolysis vapor upgrading process. ChemistrySelect 2018;3:297–307.

https://doi.org/10.1002/slct.201702431.

[52] Dos Santos N, Dulot H, Marchal N, Vrinat M. New insight on competitive reactions during deep HDS of FCC gasoline. Appl Catal A Gen 2009;352:114–23. https://doi.org/10.1016/j.apcata.2008.09.035.

[53] Anabtawi JA gregdffds., Ali SA, Abdul Bari Siddiqui M, Javaid Zaidi SM. Factors influencing the performance of naphtha hydro-desulfurization catalysts. Catal. Pet. Refin. Petrochemical Ind. 1995, 1996, p. 225–34. https://doi.org/10.1016/S0167-2991(96)80023-1.

[54] Si X, Xia D, Xiang Y, Zhou Y. Effect of H2S on the transformation of 1-hexene over NiMoS/γ-Al2O3 with hydrogen. J Nat Gas Chem 2010;19:185–8. https://doi.org/10.1016/S1003-9953(09)60054-2.

[55] Mortensen PM, Gardini D, Damsgaard CD, Grunwaldt J-D, Jensen PA, Wagner JB, et al. Deactivation of Ni-MoS_2 by bio-oil impurities during hydrodeoxygenation of phenol and octanol. Appl Catal A Gen 2016;523:159–70. https://doi.org/10.1016/j.apcata.2016.06.002.

[56] Leflaive P, Lemberton JL, Pérot G, Mirgain C, Carriat JY, Colin JM. On the origin of sulfur impurities in fluid catalytic cracking gasoline - Reactivity of thiophene derivatives and of their possible precursors under FCC conditions. Appl Catal A Gen 2002;227:201–15. https://doi.org/10.1016/S0926-860X(01)00936-X.

[57] Corma A, Martínez C, Ketley G, Blair G. On the mechanism of sulfur removal during catalytic cracking. Appl Catal A Gen 2001;208:135–52. https://doi.org/10.1016/S0926-860X(00)00693-1.

[58] Syntek Global Inc. Technical information: ASTM D975 diesel fuel specification test n.d. http://emotor-extreme.cl/assets/astm_d975_specification_test.pdf (accessed May 17, 2019).

[59] Mabanaft. Sulphur free diesel BS EN 590:2013 2015. https://www.mabanaft.com/fileadmin/content/global_content/downloads/mabanaft/Mabanaft-Ltd_Prod-Spec_Diesel.pdf (accessed May 17, 2019).

712 [60] Stanislaus A, Marafi A, Rana MS. Recent advances in the science and technology of ultra low sulfur
713 diesel (ULSD) production. Catal Today 2010;153:1–68. https://doi.org/10.1016/j.cattod.2010.05.011.

714 [61] D'Ippolito V, Andreozzi GB, Bersani D, Lottici PP. Raman fingerprint of chromate, aluminate and
715 ferrite spinels. J Raman Spectrosc 2015;46:1255–64. https://doi.org/10.1002/jrs.4764.

716 [62] Hu H, Wachs IE. Surface structures of supported molybdenum oxide catalysts. Characterization by
717 raman and Mo L3-edge XANES. J Phys Chem 1995;99:10897–910.
718 https://doi.org/10.1021/j100027a034.

719 [63] Jeziorowski H, Knözinger H. Raman and ultraviolet spectroscopic characterization of molybdena on
720 alumina catalysts. J Phys Chem 1979;83:1166–73. https://doi.org/10.1021/j100472a012.

721 [64] Hardcastle FD, Wachs IE. Determination of molybdenum–oxygen bond distances and bond orders by
722 Raman spectroscopy. J Raman Spectrosc 1990;21:683–91. https://doi.org/10.1002/jrs.1250211009.

723 [65] Payen E, Dhamelincourt MC, Dhamelincourt P, Grimblot J, Bonnelle JP. Study of Co(or Ni)-Mo Oxide
724 Phase Transformation and Hydrodesulfurization Catalysts by Raman Microprobe Equipped with New
725 Cells. Appl Spectrosc 1982;36:30–7. https://doi.org/10.1366/0003702824638953.

726 [66] Eda K, Uno Y, Nagai N, Sotani N, Whittingham MS. Crystal structure of cobalt molybdate hydrate
727 CoMoO4· nH2O. J Solid State Chem 2005;178:2791–7. https://doi.org/10.1016/j.jssc.2005.06.014.

728 [67] Himeno S, Niiya H, Ueda T. Raman Studies on the Identification of Isopolymolybdates in Aqueous
729 Solution. Bull Chem Soc Jpn 1997;70:631–7. https://doi.org/10.1246/bcsj.70.631.

730 [68] JongZ KP de, Reinalda D, Emeis CA. Coke deposition in trickle-bed reactors during heavy oil
731 processing — Catalytic and physical effects. Stud. Surf. Sci. Catal., 1994, p. 155–66.
732 https://doi.org/10.1016/S0167-2991(08)62736-6.

733 [69] Furimsky E, Massoth FE. Deactivation of hydroprocessing catalysts. Catal Today 1999;52:381–495.

https://doi.org/10.1016/S0920-5861(99)00096-6.

[70] Olsen BK, Kügler F, Castellino F, Jensen AD. Poisoning of vanadia based SCR catalysts by potassium: Influence of catalyst composition and potassium mobility. Catal Sci Technol 2016;6:2249–60. https://doi.org/10.1039/c5cy01409c.

[71] Zheng Y, Jensen AD, Johnsson JE, Thøgersen JR. Deactivation of V2O5-WO3-TiO2SCR catalyst at biomass fired power plants: Elucidation of mechanisms by lab- and pilot-scale experiments. Appl Catal B Environ 2008;83:186–94. https://doi.org/10.1016/j.apcatb.2008.02.019.

[72] Chen JP, Yang RT. Mechanism of poisoning of the V2O5 / TiO2 catalyst for the reduction of NO by NH3. J Catal 1990;125:411–20. https://doi.org/10.1016/0021-9517(90)90314-A.

[73] Nicosia D, Elsener M, Kröcher O, Jansohn P. Basic investigation of the chemical deactivation of V2O5/WO3-TiO2 SCR catalysts by potassium, calcium, and phosphate. Top Catal 2007;42–43:333–6. https://doi.org/10.1007/s11244-007-0200-4.

[74] Klimczak M, Kern P, Heinzelmann T, Lucas M, Claus P. High-throughput study of the effects of inorganic additives and poisons on NH3-SCR catalysts-Part I: V2O5-WO3/TiO2 catalysts. Appl Catal B Environ 2010;95:39–47. https://doi.org/10.1016/j.apcatb.2009.12.007.

[75] Hansen LP, Johnson E, Brorson M, Helveg S. Growth mechanism for single- and multi-layer MoS2 nanocrystals. J Phys Chem C 2014;118:22768–73. https://doi.org/10.1021/jp5069279.